

Statistical Analysis of H I Profile Asymmetry and Shape for Nearby GalaxiesNIANKUN YU (余捻坤),^{1,2} LUIS C. HO,^{1,2} JING WANG,^{1,2} AND HANGYUAN LI¹¹Kavli Institute for Astronomy and Astrophysics, Peking University, Beijing 100871, China²Department of Astronomy, School of Physics, Peking University, Beijing 100871, China

(Received March 28, 2022; Revised xxxx, 2022; Accepted xxxx, 2022)

Submitted to ApJS

ABSTRACT

We present a uniform analysis of the integrated profile of the H I emission line of 29,958 nearby ($z < 0.06$) galaxies extracted from the ALFALFA 21 cm survey. We apply the curve-of-growth technique to derive a database of spectral parameters and robust estimates of their associated uncertainties. Besides the central velocity and total flux, the main catalog provides new measures of line width, profile asymmetry, and profile shape. For a subsample of 13,511 galaxies with optical properties available from the Sloan Digital Sky Survey, we compute inclination angle-corrected line widths, rotation velocities empirically calibrated from spatially resolved observations, and dynamical masses based on H I sizes estimated from the H I mass. To facilitate subsequent scientific applications of the database, we also compile a number of ancillary physical properties of the galaxies, including their optical morphology, stellar mass, and various diagnostics of star formation activity. We use the homogeneous catalog of H I parameters to examine the statistical properties of profile asymmetry and shape. Across the full sample, which covers a wide range of stellar masses and environments, statistically significant H I profile asymmetry is detected in $\sim 20\%$ of the galaxy population. The global H I profiles are $35.2 \pm 0.3\%$ single-peaked, $26.9 \pm 0.3\%$ flat-topped, and $37.9 \pm 0.3\%$ double-horned. At a given inclination angle, double-horned profiles are preferentially associated with galaxies of higher stellar mass or optical concentration, while galaxies of lower mass or concentration tend to have single-peaked profiles.

Keywords: Galaxies: fundamental parameters - galaxies: ISM - galaxies: kinematics and dynamics - radio lines, H I 21 cm

1. INTRODUCTION

The integrated 21 cm H I spectrum of a galaxy encodes valuable information about its internal and external properties. Apart from basic data on radial velocity, neutral atomic hydrogen gas mass, and rotation velocity, which are critical for many astrophysical and cosmological applications (e.g., Tully & Fisher 1977; Haynes et al. 2018; Koribalski et al. 2004; Meyer et al. 2004; Springob et al. 2005; Wang et al. 2020), the detailed shape and asymmetry of the line profile also serve as effective tracers of galaxy kinematics and dynamics.

The extended and fragile H I disk can be distorted easily by external perturbations, such as tidal interactions (Hess et al. 2017; Sorgho et al. 2017; Bok et al. 2019), ram pressure stripping (Scott et al. 2010; Kenney et al. 2015), and gas accretion (Bournaud et al. 2005). The gas distribution also responds internally to feedback from stars (Ashley et al. 2017) and active

galactic nuclei (Morganti 2017), and the non-axisymmetric gravitational potential from spiral arms (Laine & Gottesman 1998) and bars (Saha et al. 2007; Newnham et al. 2020).

The asymmetry of the integrated H I profile offers a blunt yet convenient tool to quantify the degree of dynamical perturbation on the galactic H I disk (e.g., Richter & Sancisi 1994; Haynes et al. 1998; Andersen & Bershadsky 2009). It has been widely used historically. Measurement techniques vary greatly, from simple visual inspection (Richter & Sancisi 1994) to quantitative prescriptions based on flux (e.g., Haynes et al. 1998; Matthews et al. 1998; Bournaud et al. 2005; Espada et al. 2011), line width (e.g., Andersen & Bershadsky 2009), and central velocity (e.g., Haynes et al. 1998; Deg et al. 2020). The various asymmetry parameters typically are correlated with each other (Haynes et al. 1998; Andersen & Bershadsky 2009).

Several complications affect the interpretation of previous investigations of H I asymmetry. Besides the difficulty of comparing measurements made using disparate asymmetry parameters, there is also no commonly adopted quantitative criteria for the level of asymmetry that is deemed significant. Systematic biases due to signal-to-noise ratio (S/N) may be

important, but, with a few exceptions (e.g., [Watts et al. 2020](#)), these biases are usually neglected. Sample selection also matters, for the H I properties of galaxies vary strongly across the diverse galaxy population and the wide range of environments that they inhabit ([Saintonge & Catinella 2022](#)). These factors present a challenge to assessing the prevalence of H I asymmetry in the galaxy population. For instance, early studies have reported an asymmetry fraction of more than 50% among isolated galaxies (e.g., [Richter & Sancisi 1994](#); [Haynes et al. 1998](#); [Matthews et al. 1998](#)), which supports the notion that a galaxy’s asymmetric gas distribution is long-lived ([Baldwin et al. 1980](#); [Richter & Sancisi 1994](#)). However, other studies find much lower asymmetry fractions ($\sim 10\% - 30\%$; [Bournaud et al. 2005](#); [Espada et al. 2011](#); [Bok et al. 2019](#); [Watts et al. 2020](#)), even in cluster environments ($16\% - 26\%$; [Scott et al. 2018](#)) and among galaxy pairs ($13\% - 27\%$; [Bok et al. 2019](#); [Zuo et al. 2022](#)). The lack of consensus on the observational results has sparked debate on the physical drivers of profile asymmetry and their dependence on environment ([Espada et al. 2011](#); [Reynolds et al. 2020](#); [Watts et al. 2020](#)).

In contrast to asymmetry, for which an extensive body of work exists, relatively less attention has been devoted to characterizing the shape of the H I line profile, or to discussion of its significance. It is readily apparent that the integrated profile of the 21 cm line generally falls into one of three generic types—single-peaked, flat-topped, and double-horned—and various schemes have been developed to quantify them (e.g., [Shostak 1977](#); [Stewart et al. 2014](#); [Westmeier et al. 2014](#); [El-Badry et al. 2018](#); [Dutton et al. 2019](#); [Yu et al. 2020](#)). With few exceptions (e.g., [El-Badry et al. 2018](#)), however, the diagnostic potential contained in the profile shape has been rarely exploited. To first order, the shape of the H I profile is determined by the inclination angle along the line-of-sight and the velocity and spatial distribution of the line-emitting gas. Even in the absence of any spatial resolution, [Yu et al. \(2022b\)](#) demonstrate that useful statistical inferences can be placed on the spatial distribution of the H I using a sufficiently large sample of galaxies once certain global properties can be constrained.

In the last two decades, a number of single-dish surveys have secured global H I spectra for tens of thousands of galaxies, chief among them the H I Parkes All-Sky Survey (HIPASS; [Koribalski et al. 2004](#); [Meyer et al. 2004](#); [Wong et al. 2006](#)), the GALEX Arecibo SDSS Survey (xGASS; [Catinella et al. 2008, 2012, 2013, 2018](#)), and the Arecibo Legacy Fast ALFA survey (ALFALFA; [Haynes et al. 2011, 2018](#)). With over 31,000 detections, the ALFALFA survey is the largest blind H I survey to date. Although the sample is biased in favor of star-forming galaxies (e.g., [Huang et al. 2012](#); [Zhang et al. 2019](#)), which are more H I-rich than typical nearby galaxies ([Catinella et al. 2010, 2018](#)) or galaxies in the Virgo cluster ([Cortese et al. 2011](#)), ALFALFA nonetheless offers an opportunity to revisit the aforementioned issues, which have previously been handicapped by small-number statistics. A homogeneous, systematic analysis of the ALFALFA database paves the way for even more ambitious

exploration using upcoming surveys by the Square Kilometre Array (SKA; [Dewdney et al. 2009](#)) and its pathfinders (e.g., ASKAP; [Johnston et al. 2007](#), WALLABY; [Koribalski et al. 2020](#)), the Five-hundred-meter Aperture Spherical radio Telescope (FAST; [Nan et al. 2011](#)), and Apertif ([Adams et al. 2018](#)).

This work utilizes the curve-of-growth (CoG) method developed by [Yu et al. \(2020\)](#) to perform a uniform analysis of the H I spectra of all galaxies reliably detected by ALFALFA that also have secure optical counterparts. Our primary aim is to extract robust parameters to quantify the line asymmetry and the profile shape, paying special attention to estimating and correcting for systematic uncertainties. For the subset of galaxies that overlap with the Sloan Digital Sky Survey (SDSS; [York et al. 2000](#)), we take advantage of the ancillary optical information to derive useful physical parameters such as rotation velocities and dynamical masses, as well as compiling stellar masses (M_*), star formation rates (SFRs), and other stellar population diagnostics that will serve as the foundation for forthcoming scientific applications of this database.

We describe our sample construction in Section 2. Section 3 presents the spectral measurements, error analysis, corrections for systematic uncertainties, and comparison with the literature. Statistical results on profile asymmetry and shape are highlighted in Section 4. Section 5 summarizes our main conclusions.

2. SAMPLE

2.1. The ALFALFA Survey

The ALFALFA survey is the largest and most sensitive blind H I survey to date, having detected 31,502 nearby objects with $z < 0.06$. The ALFALFA survey used the seven-horn Arecibo L-band Feed Array (ALFA) and the drift-scan mode to map $\sim 7000 \text{ deg}^2$ with a beam size of $3'3 \times 3'8$. The survey covered two sky areas at high Galactic latitude, one in the northern and another in the southern Galactic hemisphere¹. The survey blindly searched for line emission within the frequency range 1335 – 1435 MHz, which corresponds to the heliocentric velocities $-2000 \text{ km s}^{-1} < cz < 18,000 \text{ km s}^{-1}$. The on-source integration time of $\sim 48 \text{ s}$ per beam solid angle reached a noise level of 1.6 mJy. With a channel width (δV) of 5.5 km s^{-1} , the final smoothed velocity resolution is 10 km s^{-1} , after Hanning smoothing. The survey had three data releases, covering 40%, 70%, and 100% of the final survey area, respectively ([Haynes et al. 2011, 2018](#)). This study uses 31,501 spectra from the final data release².

Except for 344 optically dark objects, the ALFALFA team identified the optical counterpart for each H I detection by considering its position, optical color, and morphology from available catalogs and databases, such as the SDSS, SkyView

¹ The survey areas are $07^h30^m < \text{R.A.} < 16^h30^m$, $0^\circ < \text{Decl.} < +36^\circ$ and $22^h < \text{R.A.} < 03^h$, $0^\circ < \text{Decl.} < +36^\circ$, where R.A. and Decl. are the equatorial coordinates (J2000).

² We omit AGC 715637 because its spectrum is in pure absorption.

(McGlynn & Scollick 1994), the Second Palomar Observatory Digital Sky Survey (POSS-II; Djorgovski et al. 1998), and the NASA Extragalactic Database (NED)³. The accuracy of optical positions assigned by ALFALFA are normally 3'' or better (Haynes et al. 2011). The survey contains 25,433 sources of quality code 1 and 6068 of quality code 2. Code 1 refers to detections with the highest quality, which is assessed by (a) consistent signal characteristics between the two independent polarizations, (b) a well-defined spatial extent that is consistent with or larger than the telescope beam, (c) spectral profile relatively free from radio frequency interference (RFI), and (d) a minimum S/N of ~ 6.5 , which is required for a detection reliability of 95% (Saintonge 2007). No constraints are placed on having a matching optical redshift. Code 2 includes objects with $S/N \lesssim 6.5$, but it must have an optical counterpart with a known optical redshift coincident with that measured in H I.

The ALFALFA catalog (Haynes et al. 2018) tabulates measurements of the total line flux, central velocity (V_{ca}), and line widths at 20% (W_{20}) and 50% (W_{50}) of the line peak. For each source, the minimum and maximum line widths measured by the ALFALFA team are denoted by $W_{\text{min}} = \min(W_{20}, W_{50})$ and $W_{\text{max}} = \max(W_{20}, W_{50})$, respectively. For galaxies with $V_{\text{ca}} \geq 6000 \text{ km s}^{-1}$, galaxy distances are computed from cz_{CMB}/H_0 , where cz_{CMB} is the recession velocity measured in the cosmic microwave background reference frame (Lineweaver et al. 1996) and $H_0 = 70 \text{ km s}^{-1} \text{ Mpc}^{-1}$ is the Hubble constant. If $V_{\text{ca}} < 6000 \text{ km s}^{-1}$, distances derive from literature analysis of the peculiar motions of galaxies, groups, and clusters (Masters 2005; Mei et al. 2007; Springob et al. 2007; Hallenbeck et al. 2012) and the Tully–Fisher relation (Tully et al. 2013).

2.2. The Main Sample

Figure 1 gives a flowchart of our process of sample construction. Starting from the original ALFALFA catalog of 31,501 galaxies, we applied the following additional selection steps to derive a main sample of 29,958 galaxies.

- We remove 344 objects without optical counterparts. From Haynes et al. (2011), these objects typically have code 1 and flag “U”, which means that they have $S/N \gtrsim 6.5$ and lie within the SDSS DR7 footprint but do not have an identified optical counterpart. Most of these objects are probably tidal dwarfs, low-surface brightness dwarfs (Jones et al. 2019), or tidal debris (Durbala et al. 2020). An object that belongs to this category AGC 229101, which Leisman et al. (2021) associated with a faint, blue galaxy with an H I-to-stellar mass ratio of ~ 100 , possibly formed through tidal interaction with neighboring objects or merged from two dark H I clouds. Due to the unknown nature and optical properties of these objects, we exclude them from subsequent analysis.

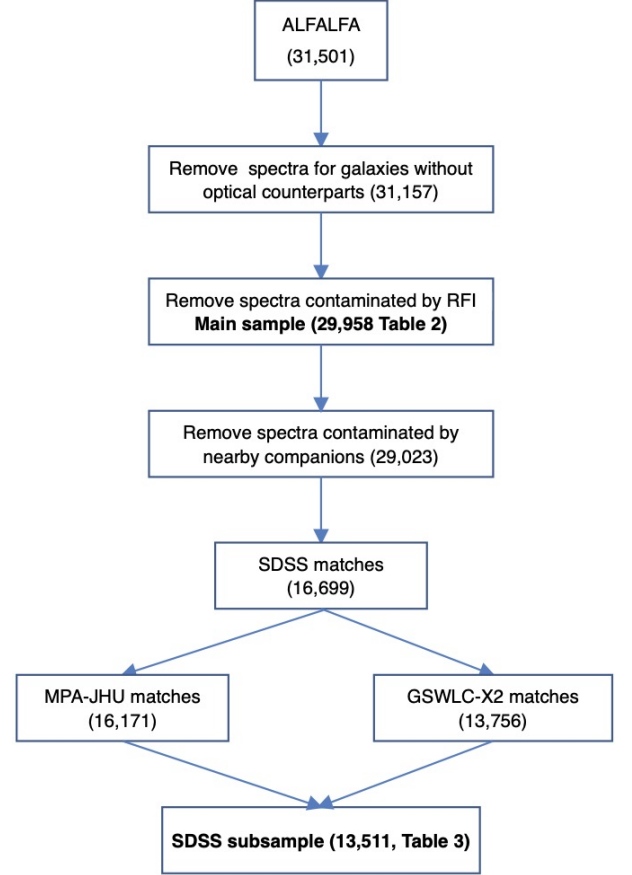


Figure 1. Flowchart of sample selection process.

- We remove 1199 galaxies strongly contaminated by RFI. We use the spectral weight to evaluate the level of RFI contamination in each channel. The minimum acceptable spectral weight is 0.5 (Haynes et al. 2018), and a spectral weight larger than 0.9 (Giovannelli et al. 2007) implies that $\sim 85\%$ of the total band pass is free of RFI. We reject spectra having bad channels with velocities within $V_{\text{ca}} \pm W_{\text{min}}/2$, or within $[V_{\text{ca}} - W_{\text{max}}, V_{\text{ca}} - W_{\text{min}}/2]$ or $[V_{\text{ca}} + W_{\text{min}}/2, V_{\text{ca}} + W_{\text{max}}]$ and the fraction of bad channels is more than 30% or the standard deviation of bad channels exceeds twice the spectral noise level. Spectra affected by a low fraction of outlying bad channels are kept but flagged by “r”.

Within the main sample, we take special care to identify 935 galaxies whose H I spectra are potentially blended by that of nearby companions. The velocity difference of two galaxies in merger pairs is smaller than 500 km s^{-1} (e.g., Patton et al. 2000; Lambas et al. 2003; Ellison et al. 2008, 2010; Bok et al. 2019). We consider nearby neighbors as candidate physical companions if it has an optical position separation smaller than the Arecibo beam size of $3.5''$ and velocity difference less than 500 km s^{-1} , using the optical positions and recession velocities from the ALFALFA catalog. If the central velocity difference is smaller than the sum of $W_{\text{min}}/2$ of the target galaxy and its apparent companion,

³ <https://ned.ipac.caltech.edu>

the apparent companion is considered a candidate companion. If the central velocity difference is smaller than the sum of $3W_{\text{max}}/4$ of the target galaxy and its apparent companion, and the median value of the flux intensities in the likely overlapping channels, which lie between the two velocity centers but beyond the velocity center range $\pm W_{\text{min}}/2$ of each, is larger than the spectral noise level from the ALFALFA catalog, then the spectrum is considered to be affected by an apparent companion. In the above two situations, the H I spectra of galaxies are considered as contaminated by nearby companions. These objects, flagged by “c”, are retained in the main sample, to facilitate subsequent analysis that may or may not wish to include them, depending on the scientific goals. Galaxies having a projected neighbor within the Arecibo beam but whose H I signal does not overlap with that of the target galaxy are flagged by “p”.

2.3. The SDSS Subsample

A significant portion of ALFALFA overlaps, by design, with SDSS. This enables a variety of science applications. To exclude the effects of the confusion and contamination, we remove galaxies whose H I spectra are contaminated by nearby companions (flagged by “c”) from the main sample. We generate an SDSS-matched subsample of galaxies based on projected separation and radial velocity. We use a maximum projected optical position separation of $3''$, the typical positional accuracy of the optical counterparts in ALFALFA (Haynes et al. 2018), which can be easily satisfied by the astrometric accuracy of SDSS ($\sim 0''.1$ at $r < 22$ mag; Pier et al. 2003). We further require that there be spectroscopy available from SDSS DR16 (Ahumada et al. 2020), and that the maximum velocity difference between the H I and the optical not exceed 500 km s^{-1} , which is within the range of observed velocity offsets in bound galaxy pairs and galaxy mergers (e.g., Patton et al. 2000; Ellison et al. 2010). The optical velocities from SDSS are accurate to $\sim 30\text{--}70 \text{ km s}^{-1}$ (York et al. 2000; Ahumada et al. 2020).

We collect from SDSS DR16 basic optical properties of the galaxies, including R_{90} and R_{50} , the radii enclosing 90% and 50% of the r -band Petrosian flux, and axis ratio q in the r band. The optical concentration index, $C \equiv R_{90}/R_{50}$, describes the optical light concentration. To quantify the strength of star formation in the central region of the galaxy, we obtain from the MPA-JHU database (Kauffmann et al. 2003; Brinchmann et al. 2004) information on $\text{EW}(\text{H}\alpha)$, the H α equivalent width, which probes the average specific SFR over the past 100 Myr (Fumagalli et al. 2012; M  rmol-Quera  t   et al. 2016; Khostovan et al. 2021), D_n4000 , the ratio of the average flux density at $4000\text{--}4100 \text{ \AA}$ to that at $3850\text{--}3950 \text{ \AA}$ (Balogh et al. 1999), which is sensitive to the mean stellar age over the past 1 Gyr (Kauffmann et al. 2003), and the SFR within the $3''$ -diameter SDSS fiber (SFR_{in}^4), which is based on the extinction-corrected H α line emission

and D_n4000 . We supplement the MPA-JHU measurements with total stellar masses and SFRs from the second version of the GALEX-SDSS-WISE Legacy Catalog with the deepest photometry (GSWLC-X2) of Salim et al. (2018), who fitted the spectral energy distribution of the global photometry from the mid-infrared, optical, and ultraviolet bands. The typical uncertainties of the stellar masses and SFRs from Salim et al. (2018) are 0.042 dex and 0.064 dex, respectively. All distance-dependent quantities are scaled to the distances adopted from ALFALFA. The SFRs and stellar masses assume the stellar initial mass function of Chabrier (2003). The final SDSS-matched subsample of 13,511 galaxies is summarized in Table 3.

3. H I PROFILE MEASUREMENTS

3.1. Curve-of-Growth Analysis

Our analysis uses the CoG method of Yu et al. (2020), which integrates the flux intensity as a function of velocity from the line center outward to both the blue and red sides of the profile, to measure several non-parametric quantities to describe the H I emission line. This method is close in spirit to those of Courteau (1997) and Andersen & Bershadsky (2009). We closely follow the formalism of Yu et al. (2020), except that no additional subtraction of the baseline is necessary because the baselines of the ALFALFA spectra are already relatively clean and flat, and our quality check based on spectral weight (Section 2.2) has successfully mitigated against RFI contamination. We mirror the negative side of flux intensity distribution to the positive side and fit the resulting distribution with a Gaussian function, whose best-fit standard deviation gives an estimate of the noise level (σ_{spec}) of the spectra.

Some slight modifications are made to the automated procedure to delineate the limits of the CoG integration, optimized for and tested using ALFALFA data. We search for emission signal within a range of $\pm 500 \text{ km s}^{-1}$ around the central velocity given in the ALFALFA catalog. We first select segments of at least three consecutive channels having positive flux intensities. Designating the segment with the highest integrated flux as reference, only segments with integrated flux or mean integrated flux larger than 0.5 times the value of the reference segment are considered as candidate emission signal. Starting from the central segment, adjacent segments with separations less than 50 km s^{-1} are merged in succession, until all segments have been combined into a single final segment spanning N channels. To facilitate subsequent calculations, we pad the final segment with $0.5N$ channels on both ends, resulting in a final data array of $2N$ channels.

With the limits of integration thus defined, we calculate the flux intensity-weighted central velocity V_c and generate the CoG⁵. The total line flux F follows from the median value

⁴ At a median distance of 137 Mpc for our sample, $3''$ corresponds to $\sim 2 \text{ kpc}$.

⁵ Roughly 4% of the spectra, typically on account of their low S/N or relatively broad emission, cannot be measured automatically by the CoG method. For these objects we set the velocity ranges manually.

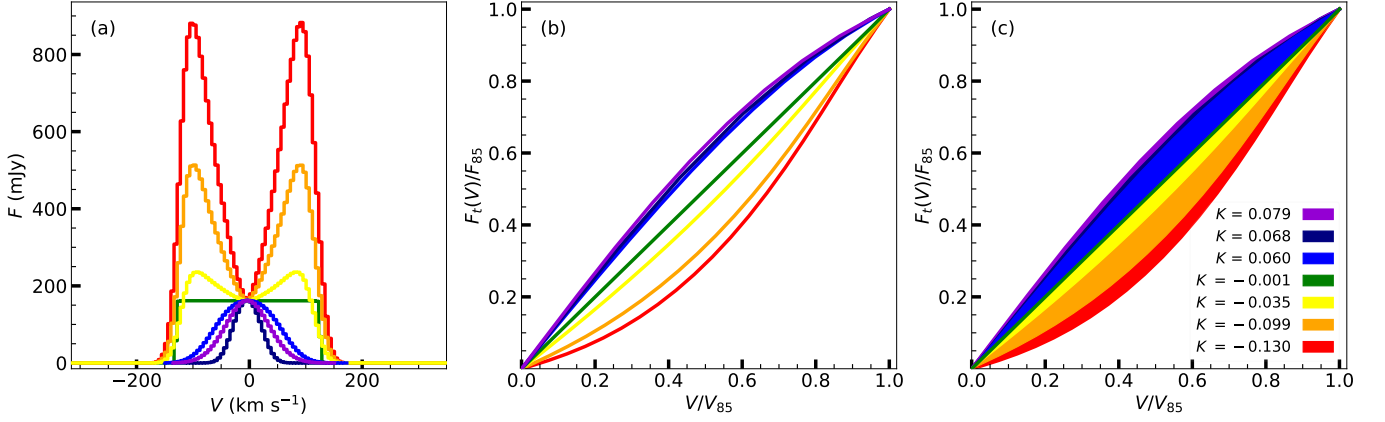


Figure 2. Illustration of the method to measure the profile shape parameter K , for (a) seven mock profiles that vary from single-peaked to flat-topped and double-horned and (b) their corresponding normalized CoGs. In panel (c), the shaded areas are the values of K , which are given in the lower-right corner of the panel; areas below the diagonal line are negative and correspond to double-horned profiles, while those above are positive and represent single-peaked profiles.

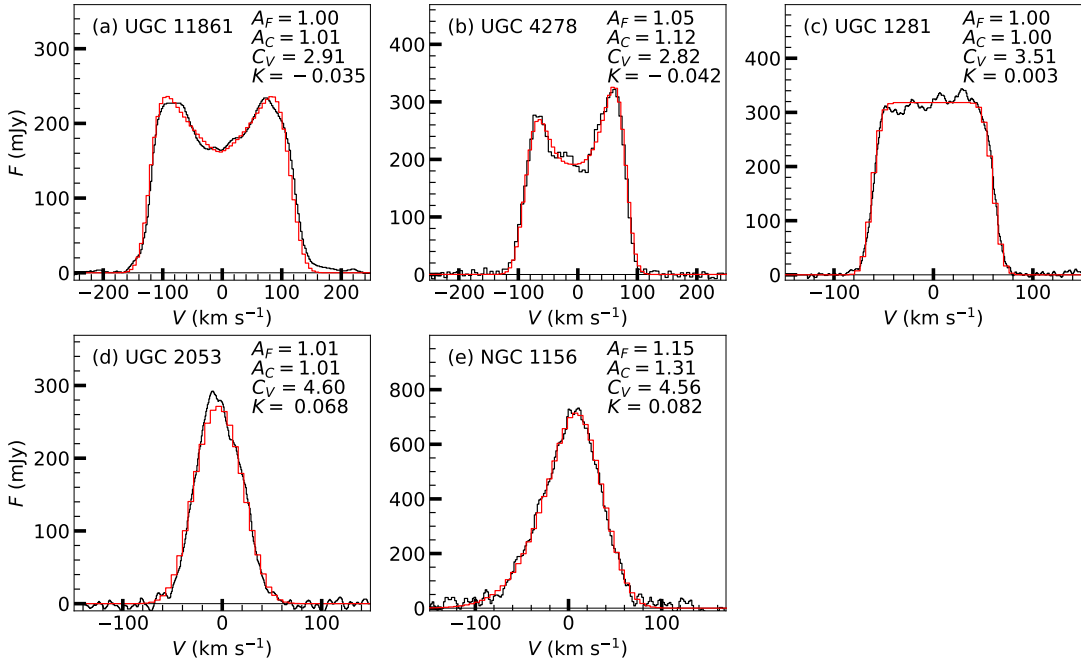


Figure 3. Illustration of five typical profile shapes, as observed (black) and fit (red) with the busy function (Westmeier et al. 2014). The profiles vary from (a) symmetric double-horned (UGC 11861) to (b) asymmetric double-horned (UGC 4278), (c) flat-topped (UGC 1281), (d) symmetric single-peaked (UGC 2053), and (e) asymmetric single-peaked (NGC 1156). The values of asymmetry and shape parameters for the mock spectra are shown in the upper-right corner.

of the flat part of the CoG. Line widths are specified as the velocity width that encloses characteristic percentages of the total flux. This catalog provides only V_{85} , the velocity width that captures 85% of the total flux, which most effectively represents the rotation velocity of the galaxy (Yu et al. 2020). We quantify the asymmetry of the line using the red and blue sides of the CoG. The asymmetry parameter A_F is defined as the larger of the ratios of the integrated flux of the one side of the line relative to the other, while A_C is the larger

of the ratios of the slopes of the rising part of the CoG of the two sides. By definition, $A_F \geq 1$ and $A_C \geq 1$. These two asymmetry parameters are broadly equivalent to previous intensity-weighted methods (e.g., Giese et al. 2016; Deg et al. 2020). The parameter C_V is the ratio of line widths V_{85} and V_{25} , where V_{25} is the line width enclosing 25% of the total flux of the CoG. Thus, C_V characterizes the degree of concentration of the line profile: $C_V = 85/25 = 3.4$ for a flat-topped (perfectly rectangular) profile. Being non-parametric,

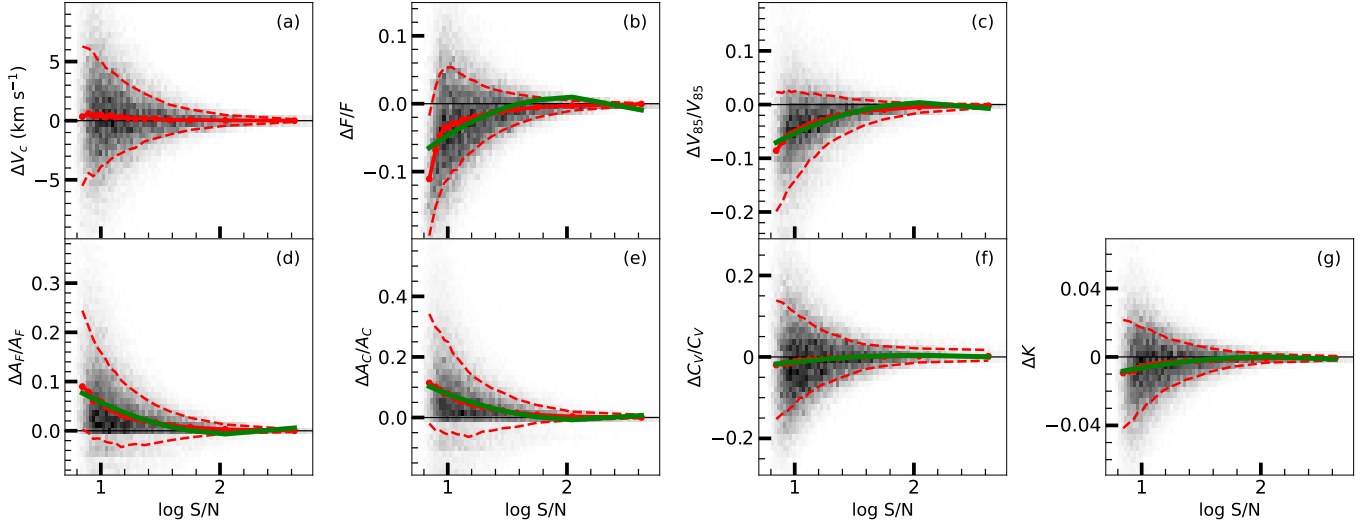


Figure 4. Simulations using mock spectra to test the sensitivity of our parameter measurements to variations in S/N. The mock spectra were generated with five types of representative profiles (flat-topped, symmetric single-peaked, asymmetric single-peaked, symmetric double-horned, and asymmetric double-horned). The panels plot (a) absolute deviations for central velocity V_c and fractional deviations for (b) flux F , (c) velocity width V_{85} , (d) flux asymmetry A_F , (e) flux distribution asymmetry A_C , (f) profile concentration C_V , and absolute deviation for (g) profile shape K . The black horizontal line denotes zero offset. The red solid lines show the median, and the dashed lines show the 16th and 84th percentiles of the distribution. Green curves in panels (b)–(g) are polynomial fits to the median distribution of total flux, line widths, asymmetry, and profile shape parameters (Equation 1).

C_V affords a more stable and less model-dependent description of the profile shape than other choices (e.g., [Stewart et al. 2014](#); [Westmeier et al. 2014](#)).

Here we introduce another new, non-parametric measure of profile shape, one that can discern even more subtle features of the line profile than C_V . Normalizing the CoG by V_{85} and the integrated flux to 85% of the total flux, we define the profile shape K as the integrated area between the normalized CoG and the diagonal line of unity in Figure 2b; K is positive or negative if the normalized CoG is above or below the line of unity. To illustrate how the profile shape influences K , we simulate seven typical H I profiles (Figure 2a) using the “busy function” ([Westmeier et al. 2014](#)) and show their normalized CoGs in Figure 2b. As can be seen from Figure 2c, a double-horned profile yields $K < 0$, a perfectly flat-topped profile gives $K = 0$, while a single-peaked line results in $K > 0$. With increasing K , the line shape transitions from a broad, double-horned profile to a narrow, single-peaked profile.

The parameters C_V and K quantify the profile shape: larger values correspond to larger profile concentration. The H I profile shape is, to the first order, governed by the inclination angle of the disk and the velocity and spatial distribution of the gas ([El-Badry et al. 2018](#)). In a companion paper, [Yu et al. \(2022b\)](#) use the present catalog to investigate the connection between H I distribution and star formation activity in nearby galaxies.

3.2. Uncertainty Estimation and Systematic Corrections

The parameters derived in this paper are affected by both statistical and systematic uncertainties. The statistical uncer-

Table 1. Measurement Uncertainties

Parameter	Systematic	Systematic	Statistical
	(5 < S/N < 10) (S/N ≥ 10)		
(1)	(2)	(3)	(4)
V_c	6.0	3.0	2.8
F	10%	5%	4%
V_{85}	12%	6%	3%
A_F	12%	7%	4%
A_C	20%	10%	6%
C_V	14%	7%	5%
K	0.029	0.015	0.011

NOTE—Col. (1): Measured parameter. The uncertainties for V_c and K are absolute, while those for the other parameters are fractional. Col. (2): Typical systematic uncertainties due to S/N if 5 < S/N < 10. Col. (3): Typical systematic uncertainties due to S/N if S/N ≥ 10. Col. (4): Typical statistical uncertainties derived from Monte Carlo simulations.

tainties for the parameters of each spectrum are estimated from a set of 50 mock spectra by adding to the original spectrum random noise following a Gaussian distribution with standard deviation equivalent to the noise level σ_{spec} . The mock spectra are analyzed in the same way as the real spectra, and the standard deviation of the distribution of each parameter is taken as its statistical uncertainty.

Several sources of systematic uncertainty need to be considered. We generate mock spectra to quantify the system-

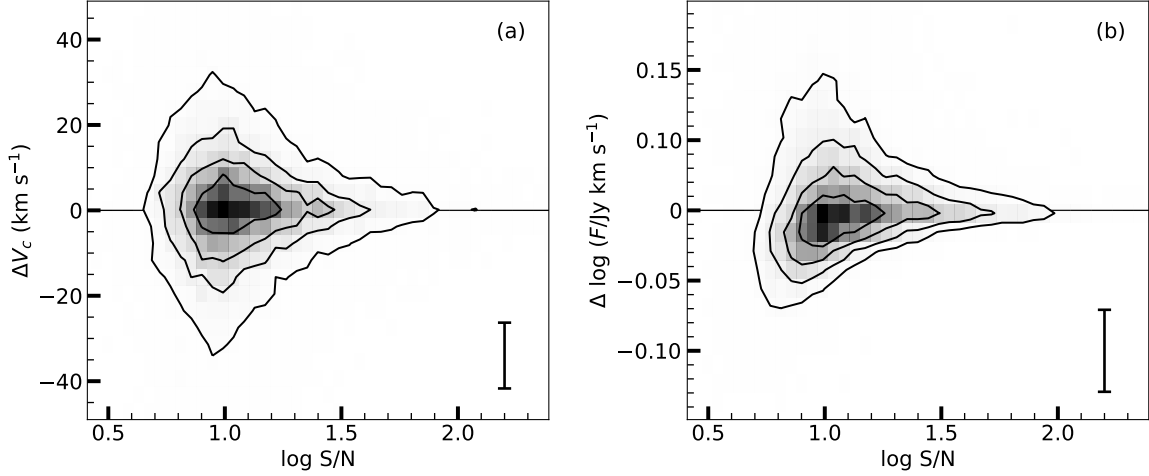


Figure 5. Comparison between our measurements of (a) central velocity V_c and (b) total flux F with measurements from the ALFALFA catalog, as a function of the S/N derived by the CoG method. Representative error bars are given in the bottom-right corner of each panel. The contours in each panel show the levels of sample inclusion, which vary from 20%, 40%, 60%, and 80% from inside out.

atic effect of spectral noise on our parameter measurements. As in Yu et al. (2020), we use the busy function (Westmeier et al. 2014) to fit the observed spectra of five galaxies whose H I spectra span a diversity of observed profile shapes, from flat-topped to symmetric single-peaked, asymmetric single-peaked, symmetric double-horned, and asymmetric double-horned. The observed H I spectra (NGC 1156: Dickel & Rood 1978; UGC 2053, UGC 1281, UGC 11861: Tifft & Cocke 1988; UGC 4278: Huchtmeier et al. 2005), along with their busy function fits, are shown in Figure 3. The derived values of profile asymmetry and shape approximately evenly cover more than 60% of the parameter distributions of the entire survey (see Figures 7 and 8). As with ALFALFA, the spectra have a channel width of 5.5 km s^{-1} . We add noise and generate 10^4 mock spectra with $S/N \approx 5$ to 600. We derive CoG parameters for the mock spectra, and then compare the recovered parameters with the input values, as a function of S/N (Figure 4).

The measurements of central velocity show no systematic deviation, although the scatter becomes predictably larger with decreasing S/N. By contrast, both the total flux and line width are underestimated slightly ($\lesssim 10\%$) at low S/N, owing to the loss of the faint wings of the line profile in noisy spectra. The asymmetry parameters A_F and A_C are systematically overestimated with decreasing S/N, consistent with the finding of Watts et al. (2020) for a differently defined asymmetry parameter, but the systematic bias never exceeds 10% for $S/N \gtrsim 5$. The profile shape parameters are systematically underestimated, although the effect is quite marginal ($\lesssim 2\%$ for C_V and $\lesssim 0.01$ for K). We also evaluate the systematic effects of adopting different criteria to detect segments for constructing the CoG (Section 3.1). In practice, we explore a range of choices of the threshold or mean flux ratio (relative to the brightest segment) and the velocity separation between two adjacent segments, perturbing their values around the fiducial default values. We conclude that the uncertainties introduced by these criteria are negligible com-

pared with other sources of uncertainty, and hence we neglect it from further consideration. While our method of error analysis is identical to that in Yu et al. (2020), the final systematic uncertainties are smaller in the current study because of improvements made to the signal selection algorithm for the CoG analysis (see Section 3.1).

In light of the detectable and quantifiable systematic uncertainties identified for the measurements of total flux, line width, asymmetry, and profile shape, we correct for the systematic biases by fitting a second-order polynomial to the median trends obtained from the mock tests (green curves in Figure 4). The corrections, applied only to spectra with $S/N < 40$ (the corrections are negligible for higher S/N), are as follows:

$$\begin{aligned}
 \Delta F/F &= -0.053(\log S/N)^2 + 0.216 \log S/N - 0.210 \\
 \Delta V_{85}/V_{85} &= -0.045(\log S/N)^2 + 0.193 \log S/N - 0.201 \\
 \Delta A_F/A_F &= 0.051(\log S/N)^2 - 0.216 \log S/N + 0.223 \\
 \Delta A_C/A_C &= 0.065(\log S/N)^2 - 0.281 \log S/N + 0.293 \\
 \Delta C_V/C_V &= -0.014(\log S/N)^2 + 0.059 \log S/N - 0.057 \\
 \Delta K &= -0.005(\log S/N)^2 + 0.022 \log S/N - 0.023.
 \end{aligned} \tag{1}$$

Unless otherwise noted, we correct the above parameters for these systematic deviations.

The final error budget of each parameter is the quadrature sum of the statistical uncertainties and systematic uncertainties, as summarized in Table 1. Following Springob et al. (2005), we include an additional uncertainty of 15% for the total flux, to account for H I self-absorption and calibration-related effects (beam attenuation, pointing, and flux calibration).

3.3. Comparison with ALFALFA

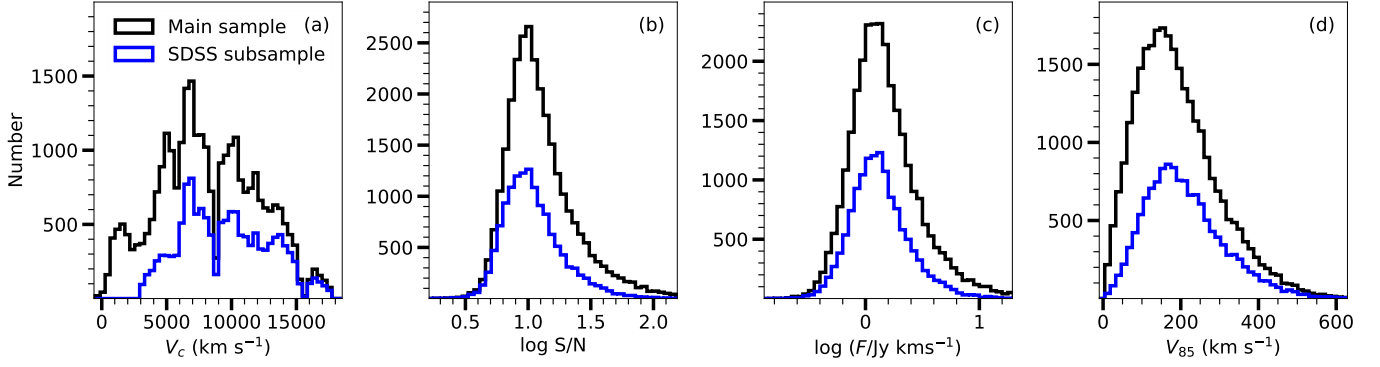


Figure 6. Distribution of (a) central velocity V_c , (b) S/N, (c) total flux F , and (d) observed velocity width V_{85} for the main sample (black) and SDSS subsample (blue).

We use the published ALFALFA catalog as an independent verification of our measurements. This is possible only for the central velocity and the total flux. The other parameters are either new to our study (e.g., profile shape), not uniformly measured (e.g., asymmetry), or are defined differently (e.g., line widths). Our central velocity V_c is defined as the flux intensity-weighted central velocity, while the central velocity in the ALFALFA catalog is the midpoint of the channels with flux intensity equal to the 50% level of each of the two peaks. Our total flux is derived by calculating the median integrated flux on the flat part of the CoG, which differs from the approach employed by ALFALFA. Nevertheless, the two sets of measurements show no obvious systematic discrepancies with respect to each other (Figure 5). The scatter increases from $\Delta V_c = 0.4 \pm 7.0 \text{ km s}^{-1}$ for $S/N \geq 10$ to $\Delta V_c = 0.0 \pm 10.8 \text{ km s}^{-1}$ for $S/N < 10$. As for the line flux, $\Delta \log F = 0.00 \pm 0.01 \text{ dex}$ for $S/N \geq 10$, with the scatter and standard deviation increasing to $\Delta \log F = 0.00 \pm 0.03 \text{ dex}$ for $S/N < 10$. The scatter is consistent with the typical uncertainties in Table 1.

3.4. Final Measurements and Derived Physical Properties

Figure 6 summarizes the basic properties of the main sample and SDSS subsample. For the main sample, central velocities range from $V_c \approx 0$ to $18,000 \text{ km s}^{-1}$, which correspond to redshifts $z \approx 0 - 0.06$. The spectra vary greatly in quality, from $S/N \approx 4$ to more than 100, with integrated H I fluxes spanning $F = 0.25$ to 10 Jy km s^{-1} . The observed velocity widths cluster near $V_{85} \approx 200 \text{ km s}^{-1}$, with some as low as 50 km s^{-1} and a long tail stretching out to $\sim 500 \text{ km s}^{-1}$, which may be due to confusion from unrecognized nearby sources (e.g., Brosch et al. 2011). The principal parameters measured for the main sample are given in Table 2.

The SDSS subsample closely matches the main sample in its general characteristics (Figure 6, blue histograms). The redshift range of the SDSS subsample is $z \approx 0.01 - 0.06$, which is mainly constrained by the matching with GSWLC-X2. The availability of ancillary optical data allows us to deduce a number of useful physical properties for the galaxies (Table 3). Of chief importance is the optically derived axis ratio, $q = b/a$, which can be used to estimate the in-

clination angle (i) of the galaxy. Following Hubble’s (1926) prescription,

$$\cos^2 i = \frac{q^2 - q_0^2}{1 - q_0^2}, \quad (2)$$

where q_0 is the intrinsic disk thickness. We estimate q_0 from the stellar mass following Sánchez-Janssen et al. (2010). We assume that the H I disk is coplanar with the stellar disk. This is generally a reasonably good assumption in most galaxies (e.g., Verheijen & Sancisi 2001), even though in some early-type galaxies the stars and H I can be severely misaligned (e.g., Morganti et al. 2006). We correct the observed velocity width for the effects of projection, redshift, instrumental resolution, and turbulence broadening (Yu et al. 2020),

$$V_{85c} = \frac{(V_{85} - V_{\text{inst}})/(1 + z) - V_{\text{turb}}}{2 \sin i}, \quad (3)$$

where V_{inst} and V_{turb} are line-width correction terms for the instrumental resolution and turbulence motion, respectively. At a given instrumental resolution (10 km s^{-1} ; Haynes et al. 2018) and turbulence velocity dispersion (10 km s^{-1} ; Lelli et al. 2016), the correction terms depend on the observed line width (see Figure 6 of Yu et al. 2020).

With V_{85c} in hand, we obtain the galaxy rotation velocity (V_{rot}) from the empirical calibration outlined in Yu et al. (2020). Finally, we calculate the dynamical mass $M_{\text{dyn}} = V_{\text{rot}}^2 R/G$, assuming, as in Yu et al. (2020), that $R = R_{\text{HI}}$, the characteristic H I radius that obeys the H I mass-size relation of Wang et al. (2016).

4. RESULTS

4.1. Statistical Properties of H I Profile Asymmetry

Asymmetric gas distribution or kinematics can be induced by environmental effects (e.g., Cortese et al. 2021, and references therein), major and minor mergers (e.g., Jog & Solomon 1992; Barnes 2002; Boomsma et al. 2005; Robertson et al. 2006), gas accretion (Bournaud et al. 2005; Sancisi et al. 2008), internal perturbations by stellar feedback (Ashley et al. 2017), active galactic nuclei feedback (Morganti 2017), and non-axisymmetric perturbations to the gravitational potential (Baldwin et al. 1980; Hayashi & Navarro

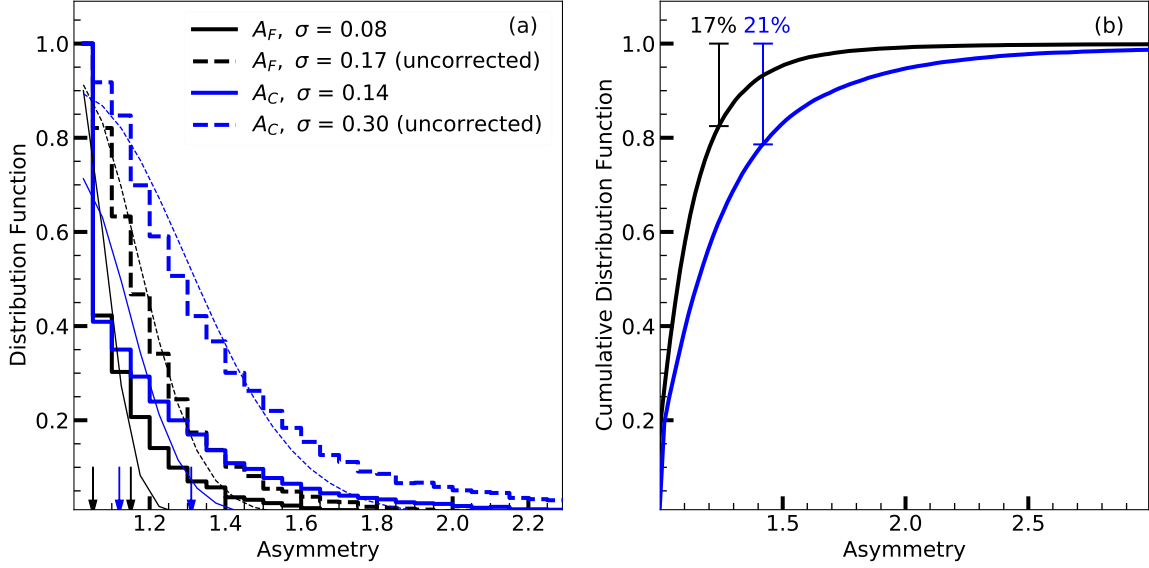


Figure 7. (a) Distribution function and (b) cumulative distribution function of the asymmetry parameters A_F (black) and A_C (blue). In panel (a), the standard deviation of the half-Gaussian fits of the distributions (thin curves) are given in the legends, and the black and blue arrows mark the values of A_F and A_C of the two asymmetry profiles in our simulations (Figures 3 and 4). The fraction of the sample that is asymmetric, defined as $A_F > 1.24$ and $A_C > 1.42$, is denoted in panel (b).

2006) due to a bar (Saha et al. 2007; Newnham et al. 2020) or spiral arms (Laine & Gottesman 1998).

Figure 7a shows the distribution of the asymmetry parameters A_F and A_C of the main sample, which is characterized by a dominant peak centered at 1, followed by a long, extended tail toward higher values. We emphasize the importance of S/N correction (Section 3.2), without which the profile asymmetry would be greatly overestimated. Fitting the corrected distribution functions with a half-Gaussian, the standard deviation is $\sigma = 0.08$ for A_F and $\sigma = 0.14$ for A_C . We define an object as asymmetric if its asymmetry parameters exceed 3σ . By this criterion, the cumulative distribution functions yield an asymmetry fraction of $\sim 20\%$ ($17.5\% \pm 0.2\%$ for A_F and $21.4\% \pm 0.2\%$ for A_C ; Figure 7b). The uncertainties for the fractions are 68.3% confidence intervals calculated for a binomial distribution (Cameron 2011). It is non-trivial to compare our results to those in the literature. While our asymmetry fractions are roughly consistent with those quoted by (Bournaud et al. 2005, 22%) and (Espada et al. 2011, 9%), they are notably lower than the $\sim 50\%$ asymmetry fractions claimed by earlier studies that were based on less stringent classification criteria for profile asymmetry (Richter & Sancisi 1994; Haynes et al. 1998; Matthews et al. 1998). Most studies (but see Watts et al. 2020) did not consider the systematic bias due to S/N.

We note that A_C has a more prominent tail toward high values than A_F ; the two parameters are significantly but not tightly correlated (Pearson’s correlation coefficient $r = 0.37$). They probe different and complimentary aspects of the H I asymmetry. Defined as the ratio of the integrated flux of the blueshifted and redshifted sides of the CoG, A_F is sensitive to the asymmetry of the edges of the line profile. On

the other hand, A_C , defined as the ratio of the slopes of the rising portion of the CoG of the two sides of the line, is more sensitive to the asymmetry within the inner 85% of the total gas distribution. The parameter A_F gauges perturbations imparted by external, environmental effects, and A_C should better reflect perturbations internal to the galaxy itself. A forthcoming work (N. Yu et al., in preparation) will investigate the dependence of H I asymmetry on the environmental and physical properties of galaxies.

4.2. Statistical Properties of H I Profile Shapes

Figure 8 shows the distribution of profile shape parameters. The shape parameters C_V and K increase when a profile changes from double-horned to flat-topped and single-peaked, centered on a value of $C_V = 3.4$ or $K = 0$ for a flat-topped profile. Given the median uncertainties for C_V (0.33) and K (0.022), we classify the line profiles into three generic types by the following criteria: single-peaked ($C_V > 3.7$, $K > 0.02$), flat-topped ($3.1 \leq C_V \leq 3.7$, $-0.02 \leq K \leq 0.02$), and double-horned ($C_V < 3.1$, $K < -0.02$). Example profiles are shown in Figure 3. According to the C_V criteria, the fractions of single-peaked, flat-topped, and double-horned profiles in the ALFALFA main sample are $36.6 \pm 0.3\%$, $27.8 \pm 0.3\%$, and $35.6 \pm 0.3\%$, respectively. The corresponding statistics adopting the K criteria are $35.2 \pm 0.3\%$, $26.9 \pm 0.3\%$, and $37.9 \pm 0.3\%$, respectively. The two parameters give quite similar fractions for the three types of profile shape. As K makes use of the full information from the CoG, and not just the ratio of two line widths used to define C_V , the former is superior to the latter as a shape indicator, and therefore we consider the statistics based on K to be more accurate.

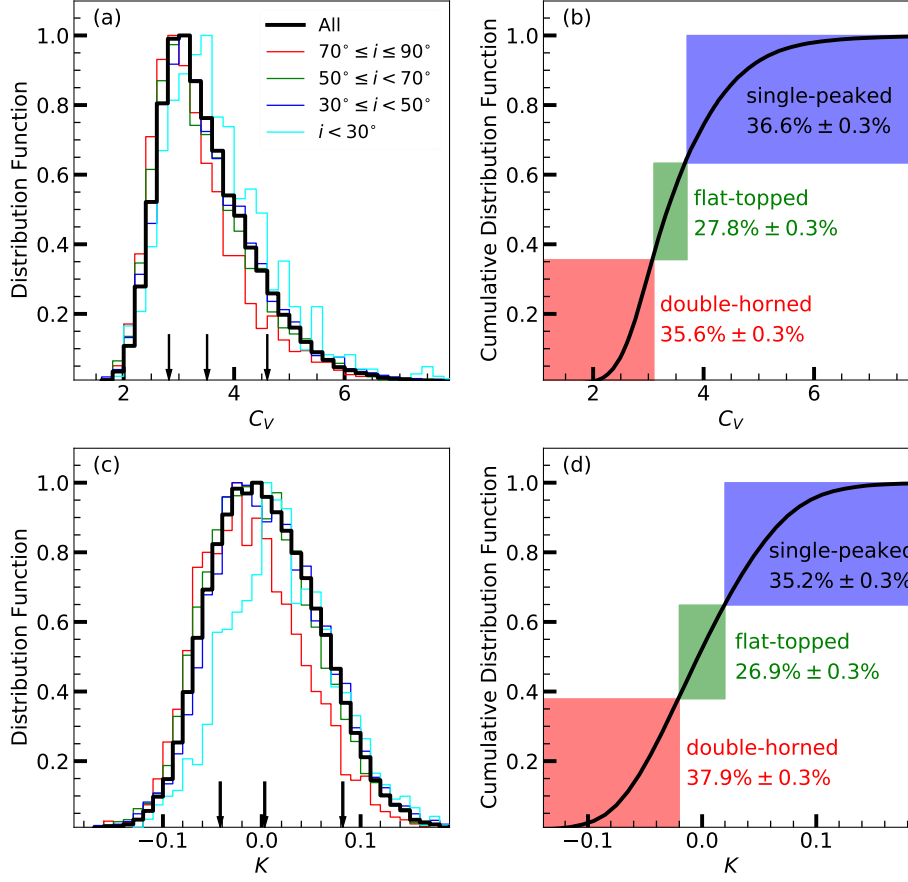


Figure 8. Distribution function (left) and cumulative distribution function (right) of the profile shape parameters C_V (top) and K (bottom). For the distribution functions, objects of the main sample are plotted (thick black histogram), as well as for SDSS subsamples binned by inclination angle: $70^\circ \leq i \leq 90^\circ$ (red), $50^\circ \leq i < 70^\circ$ (green), $30^\circ \leq i < 50^\circ$ (blue), and $i < 30^\circ$ (cyan). In panels (a) and (c), the black arrows show the values of C_V and K of three different profile shapes used in our simulations (Figures 3 and 4).

The observed line profile is affected by projection effects. An intrinsically double-horned profile, which is characteristic of most massive disk galaxies having a sufficiently extended H I distribution that samples the flat part of the rotation curve (e.g., Roberts 1978; Martinsson et al. 2016), would appear single-peaked when viewed face-on, with the width of the profile determined primarily by the turbulence motions of the H I disk. However, besides inclination angle, the H I profile also imprints the velocity and spatial distribution of the gas (El-Badry et al. 2018; Yu et al. 2022b). Thus, while more face-on systems tend to have higher values of C_V and K , such that the H I profile is more likely to be single-peaked compared to edge-on systems (Figures 8a and 8c), each of the bins of inclination angle covers a wide range of values for C_V and K .

At a given inclination angle, galaxies with a higher stellar mass or optical concentration have a greater tendency to exhibit double-horned H I profiles (lower C_V or K) compared to galaxies of lower mass or concentration (Figures 9 and 10). The formal statistical significance is not high, as judged by the Pearson’s correlation coefficients, but the trends are persistent. The overall dependence of profile shape on galaxy

stellar mass resembles a similar trend seen in the study by El-Badry et al. (2018), which was based on a sample of ~ 2000 low-redshift, H I-detected galaxies. These authors attributed the scatter in the relation between profile shape and galaxy stellar mass to inclination angle. However, our results show that the scatter is still noticeable after fixing the inclination angle to a narrow range, suggesting that the scatter may be linked to physical factors, such as H I content, H I radial distribution, and velocity field. The trends with stellar mass are stronger than those with concentration, and they are more prominent for K than for C_V . Moreover, the observed scatter of C_V and K at fixed M_* or C is substantial, and real, larger than the typical measurement uncertainties. The intrinsic scatter can be used to diagnose physical processes that can lead the H I profiles to depart from the expected norm. For example, Zuo et al. (2022) note that gas-rich, major mergers, despite being massive galaxies, have a high frequency of single-peaked H I profiles, likely a consequence of central gas inflow induced by gravitational torques.

This work represents the largest, most uniform, quantitative analysis of H I profile shapes to date. Previous statistics on the H I profile shape of nearby galaxies are not only highly

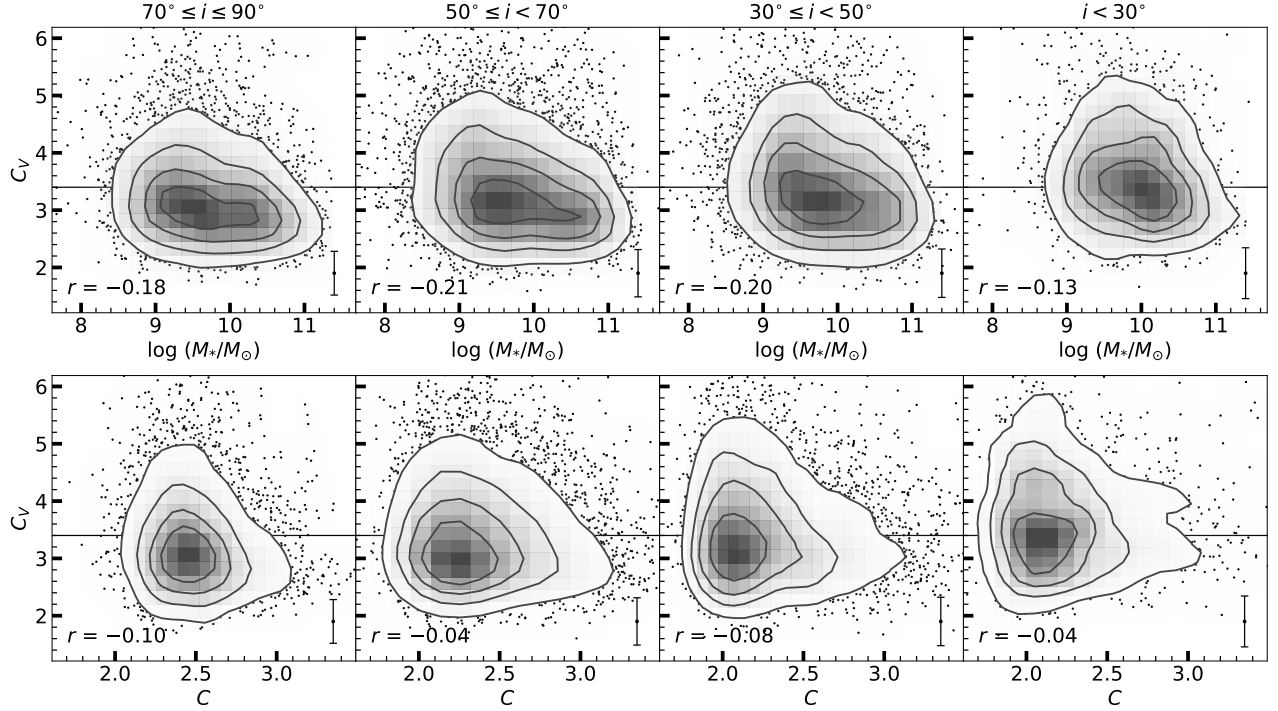


Figure 9. The variation of profile concentration C_V on (top) stellar mass M_* and (bottom) optical concentration C for subsamples binned by inclination angle: from left to right, $70^\circ \leq i \leq 90^\circ$, $50^\circ \leq i < 70^\circ$, $30^\circ \leq i < 50^\circ$, and $i < 30^\circ$. The density of points is highlighted by grayscale and contours. The Pearson's correlation coefficient and a typical error bar for C_V are given in the bottom of each panel. The contours in each panel show the levels of sample inclusion, which vary from 20%, 40%, 60%, and 80% from inside out.

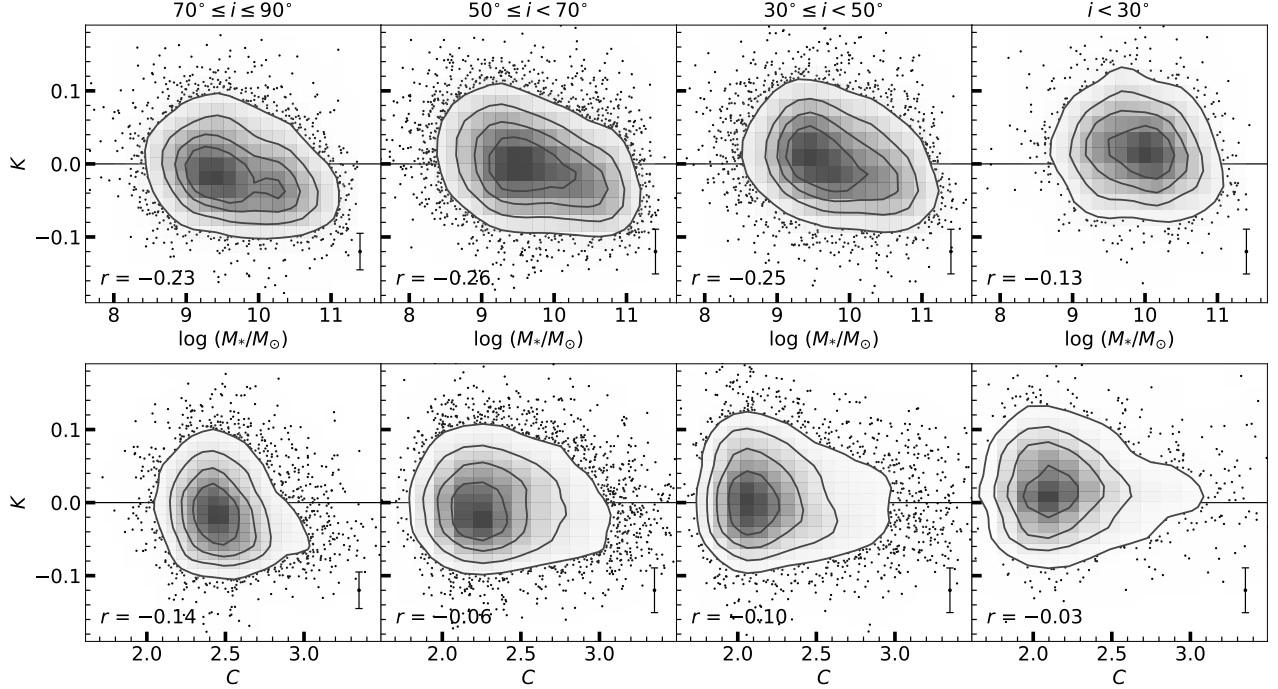


Figure 10. The variation of profile shape K on (top) stellar mass M_* and (bottom) optical concentration C for subsamples binned by inclination angle: from left to right, $70^\circ \leq i \leq 90^\circ$, $50^\circ \leq i < 70^\circ$, $30^\circ \leq i < 50^\circ$, and $i < 30^\circ$. The density of points is highlighted by grayscale and contours. The Pearson's correlation coefficient and a typical error bar for K are given in the bottom of each panel. The contours in each panel show the levels of sample inclusion, which vary from 20%, 40%, 60%, and 80% from inside out.

limited, based on fragmentary samples of $\lesssim 100$ objects, but

they also derive from subjective, visual classification (e.g., Geha et al. 2006; Ho et al. 2008b; Zhou et al. 2018).

5. SUMMARY

We apply the curve-of-growth technique of Yu et al. (2020) to perform a uniform analysis of the integrated H I 21 cm spectra of 29,958 galaxies with unambiguous optical counterparts from the ALFALFA survey. The main sample consists of nearby (median $z = 0.026$), gas-rich galaxies spanning a wide range of H I mass ($M_{\text{H I}} \approx 10^{7.2} - 10^{10.6} M_{\odot}$). Apart from basic parameters such as central velocity and total flux, the main catalog provides new measures of line width (V_{85}), profile asymmetry (A_F and A_C), and line shape (C_V and K). We identify sources that may be confused by nearby, potentially physically associated neighbors, information that itself can be used to investigate the effect of local environment or dynamical interactions. For the subsample of 13,511 galaxies that overlap with SDSS, which cover a wide range of stellar mass ($M_* \approx 10^{8.0} - 10^{11.5} M_{\odot}$, median $10^{9.7} M_*$), we provide higher level science products, including inclination angle-corrected line widths (V_{85c}), rotation velocities (V_{rot}), and dynamical masses (M_{dyn}), as well as ancillary physical properties (morphology, stellar mass, star formation activity), which will be used for a series of forthcoming applications.

The availability of a homogeneous catalog of H I parameters affords us the opportunity to reexamine the frequency of H I profile asymmetry. Across the full sample of galaxies under consideration, the fraction of galaxies with statistically significant H I profile asymmetry is $\sim 20\%$. The H I spectra exhibit diverse profile shapes, but most can be classified as single-peaked ($35.2 \pm 0.3\%$), flat-topped ($26.9 \pm 0.3\%$), or double-horned ($37.9 \pm 0.3\%$). The profile shapes reflect projection effects as well the intrinsic spatial and velocity distribution of the gas, which vary systematically with galaxy mass and mass distribution. At a given inclination angle, double-horned profiles are preferentially associated with galaxies of higher stellar mass or optical concentration, while galaxies of lower mass or concentration tend to have single-peaked profiles.

ACKNOWLEDGMENTS

We thank the anonymous referee for very helpful comments and suggestions. This work was supported by the National Science Foundation of China (11721303, 11991052, 11903003, 12073002), the China Manned Space Project (CMS-CSST-2021-A04, CMS-CSST-2021-B02), and the National Key R&D Program of China (2016YFA0400702). We thank Martha Haynes for kindly providing the spectra of ALFALFA survey. We are grateful to Pei Zuo, Yuming Fu, Jinyi Shangguan, Tianqi Huang, and Zhiwei Pan for useful advice and discussion. This research has made use of the NASA/IPAC Extragalactic Database (<http://ned.ipac.caltech.edu>), which is funded by the National Aeronautics and Space Administration and operated by the California Institute of Technology. We used Astropy, a community-developed core Python package for astronomy (Astropy Collaboration et al. (2013)).

Table 2. Parameters Derived from the H I Spectra of the Main Sample

Galaxy	R.A.	Decl.	D_L	V_c	F	V_{85}	A_F	A_C	C_V	K	S/N	σ_{spec}	$\log M_{\text{H I}}$	Notes
(1)	(2)	(3)	(4)	(5)	(6)	(7)	(8)	(9)	(10)	(11)	(12)	(13)	(14)	(15)
	($^\circ$)	($^\circ$)	(Mpc)	(km s^{-1})	(Jy km s^{-1})	(km s^{-1})							(M_\odot)	
AGC 000001	0.65667	16.65222	82.8 \pm 2.2	5832 \pm 3	2.96 \pm 0.46	154 \pm 11	1.01 \pm 0.08	1.14 \pm 0.13	5.02 \pm 0.36	0.106 \pm 0.017	21.2	2.5	9.68 \pm 0.07	1p
AGC 000004	0.73708	4.20889	118.0 \pm 2.3	8487 \pm 14	1.40 \pm 0.25	217 \pm 28	1.61 \pm 0.23	1.68 \pm 0.38	4.58 \pm 0.73	0.020 \pm 0.033	9.5	2.5	9.66 \pm 0.08	1
AGC 000006	0.79042	21.95972	88.8 \pm 2.2	6576 \pm 9	1.17 \pm 0.21	227 \pm 28	1.32 \pm 0.19	1.08 \pm 0.27	5.00 \pm 0.81	0.012 \pm 0.034	7.2	2.8	9.34 \pm 0.08	2
AGC 000007	0.79667	15.96500	155.2 \pm 2.2	11252 \pm 25	4.04 \pm 0.65	646 \pm 47	1.15 \pm 0.11	1.71 \pm 0.21	2.70 \pm 0.24	-0.055 \pm 0.018	28.2	1.9	10.36 \pm 0.07	1
AGC 000008	0.81167	16.14556	13.2 \pm 1.3	1048 \pm 3	22.42 \pm 3.55	426 \pm 26	1.02 \pm 0.07	1.06 \pm 0.11	2.92 \pm 0.20	-0.045 \pm 0.015	157.3	2.0	8.96 \pm 0.11	1
AGC 000010	0.83542	8.61861	165.4 \pm 2.1	11933 \pm 3	6.66 \pm 1.05	225 \pm 14	1.16 \pm 0.08	1.53 \pm 0.16	2.77 \pm 0.20	-0.045 \pm 0.016	32.5	3.4	10.63 \pm 0.07	1
AGC 000011	0.83958	22.10250	62.8 \pm 2.4	4443 \pm 4	2.33 \pm 0.37	211 \pm 13	1.22 \pm 0.09	1.06 \pm 0.12	2.73 \pm 0.22	-0.010 \pm 0.018	19.2	2.1	9.34 \pm 0.08	1
AGC 000012	0.83500	29.79722	95.0 \pm 2.4	6980 \pm 3	2.98 \pm 0.47	224 \pm 13	1.04 \pm 0.08	1.00 \pm 0.11	2.75 \pm 0.21	-0.047 \pm 0.015	22.5	2.2	9.80 \pm 0.07	1
AGC 000013	0.87167	27.35139	105.9 \pm 2.2	7764 \pm 7	0.81 \pm 0.15	170 \pm 24	1.02 \pm 0.16	1.15 \pm 0.29	5.19 \pm 0.83	0.140 \pm 0.035	5.8	2.9	9.33 \pm 0.08	2
AGC 000014	0.89625	23.20028	98.6 \pm 2.2	7236 \pm 3	6.74 \pm 1.07	319 \pm 20	1.13 \pm 0.08	1.40 \pm 0.14	2.57 \pm 0.18	-0.060 \pm 0.016	40.4	2.5	10.19 \pm 0.07	1
AGC 000015	0.93625	4.29806	160.1 \pm 2.1	11558 \pm 7	3.27 \pm 0.52	494 \pm 30	1.15 \pm 0.10	1.16 \pm 0.14	2.90 \pm 0.23	-0.034 \pm 0.017	18.4	2.3	10.30 \pm 0.07	1
AGC 000016	0.95375	7.47861	74.1 \pm 2.4	5245 \pm 3	11.85 \pm 1.87	153 \pm 9	1.08 \pm 0.08	1.19 \pm 0.12	2.52 \pm 0.18	-0.076 \pm 0.015	74.0	3.3	10.19 \pm 0.07	1
AGC 000017	0.93000	15.21806	20.3 \pm 4.3	876 \pm 3	6.72 \pm 1.06	87 \pm 5	1.01 \pm 0.07	1.03 \pm 0.10	3.28 \pm 0.23	-0.017 \pm 0.015	74.6	2.4	8.82 \pm 0.20	1
AGC 000021	1.03708	7.37889	87.7 \pm 2.3	6202 \pm 3	5.01 \pm 0.79	163 \pm 10	1.19 \pm 0.09	1.26 \pm 0.14	2.89 \pm 0.21	-0.044 \pm 0.015	27.9	3.4	9.96 \pm 0.07	1
AGC 000022	1.02083	10.29417	105.6 \pm 2.2	7743 \pm 7	2.98 \pm 0.47	370 \pm 23	1.00 \pm 0.07	1.09 \pm 0.14	2.77 \pm 0.22	-0.057 \pm 0.018	13.7	2.9	9.89 \pm 0.07	1
AGC 000023	1.05417	10.79028	108.8 \pm 2.2	7969 \pm 7	2.33 \pm 0.36	370 \pm 25	1.20 \pm 0.10	1.83 \pm 0.23	2.84 \pm 0.35	-0.049 \pm 0.018	16.9	2.0	9.81 \pm 0.07	1
AGC 000024	1.06125	22.58778	48.1 \pm 9.1	4446 \pm 3	5.40 \pm 0.86	162 \pm 10	1.01 \pm 0.07	1.01 \pm 0.10	3.12 \pm 0.22	-0.032 \pm 0.015	46.6	2.3	9.47 \pm 0.18	1
AGC 000025	1.10458	6.17778	78.7 \pm 15.2	5081 \pm 3	3.79 \pm 0.60	257 \pm 16	1.13 \pm 0.08	1.26 \pm 0.14	2.52 \pm 0.19	-0.060 \pm 0.016	27.4	2.3	9.74 \pm 0.18	1
AGC 000026	1.10208	31.47194	42.1 \pm 8.3	4954 \pm 3	10.23 \pm 1.62	218 \pm 13	1.01 \pm 0.07	1.04 \pm 0.10	2.80 \pm 0.20	-0.056 \pm 0.015	75.5	2.4	9.63 \pm 0.18	1
AGC 000027	1.12125	5.84556	44.5 \pm 9.2	3112 \pm 3	13.51 \pm 2.14	193 \pm 12	1.01 \pm 0.07	1.05 \pm 0.11	2.73 \pm 0.19	-0.058 \pm 0.015	138.8	1.9	9.80 \pm 0.19	1
AGC 000030	1.13625	33.55917	68.7 \pm 4.2	4761 \pm 4	2.60 \pm 0.40	224 \pm 13	1.00 \pm 0.07	1.00 \pm 0.11	2.51 \pm 0.19	-0.074 \pm 0.016	15.5	3.0	9.46 \pm 0.09	1

NOTE.—Col. (1): Galaxy name from the Arecibo General Catalog (AGC). Cols. (2)–(3): Equatorial coordinates (J2000) of the optical counterpart assigned by ALFALFA. Col. (4): Luminosity distance from the ALFALFA catalog. Col. (5): Flux intensity-weighted central velocity. Col. (6): Total integrated flux of the H I line. Col. (7): Velocity width measured at 85% of the total line flux. Col. (8): Integrated flux asymmetry. Col. (9): Flux distribution asymmetry. Col. (10): Profile concentration. Col. (11): Profile shape. Col. (12): S/N of the profile. Col. (13): Noise level of the profile. Col. (14): H I mass, following $M_{\text{H I}} = 2.36 \times 10^5 D_L^2 F M_\odot$ (Roberts 1962); for a distance uncertainty of 10% and a flux uncertainty of 15%, the typical uncertainty of $\log M_{\text{H I}}$ is 0.11 dex. Col. (15): Notes: 1 = code 1 detection; 2 = code 2 detection; r = there are data points with spectral weight less than 0.5, which are located at the edge of the emission signal; c = the H I emission overlaps with that of nearby companion(s); p = the H I emission is not confused even though there is at least a projected neighbor within the Arecibo beam. (This table is available in its entirety in machine-readable form.)

Table 3. Properties of the SDSS Subsample

Galaxy	z	R_{90} (kpc)	$R_{H\text{I}}$ (kpc)	C	b/a	i ($^\circ$)	V_{rot} (km s $^{-1}$)	$\log M_*$ (M_\odot)	$\log \text{SFR}$ ($M_\odot \text{yr}^{-1}$)	$\log \text{SFR}_{\text{in}}$ ($M_\odot \text{yr}^{-1}$)	$D_{\text{H}4000}$	$\text{EW}(\text{H}\alpha)$ (\AA)	$\log M_{\text{dyn}}$ (M_\odot)
(1)	(2)	(3)	(4)	(5)	(6)	(7)	(8)	(9)	(10)	(11)	(12)	(13)	(14)
AGC 000007	0.03742	16.0 \pm 1.1	49.5 \pm 4.1	2.8	0.4	72 \pm 5	332 \pm 45	11.342 \pm 0.014	-0.039 \pm 0.117	-2.002	1.97	1.41	12.1 \pm 0.2
AGC 000043	0.01759	4.2 \pm 0.1	16.3 \pm 1.4	2.1	0.4	69 \pm 5	97 \pm 10	9.268 \pm 0.046	-0.966 \pm 0.078	-2.030	1.20	31.58	10.5 \pm 0.2
AGC 000056	0.01809	7.0 \pm 0.1	21.2 \pm 4.5	2.0	0.7	42 \pm 5	138 \pm 16	9.814 \pm 0.029	-0.605 \pm 0.048	-2.239	1.34	5.98	11.0 \pm 0.2
AGC 000180	0.03664	17.2 \pm 0.5	27.2 \pm 2.6	2.6	0.3	76 \pm 6	199 \pm 45	11.210 \pm 0.048	0.305 \pm 0.163	-1.713	1.84	1.65	11.4 \pm 0.2
AGC 000194	0.01827	17.1 \pm 0.4	15.6 \pm 1.5	3.2	0.7	49 \pm 5	356 \pm 71	10.787 \pm 0.004	-1.249 \pm 0.033	-2.326	1.95	3.88	11.7 \pm 0.2
AGC 000219	0.01750	8.7 \pm 0.1	33.4 \pm 7.7	2.5	0.3	73 \pm 5	135 \pm 14	10.069 \pm 0.022	-0.358 \pm 0.037	-2.134	1.42	8.47	11.1 \pm 0.2
AGC 000230	0.01771	8.8 \pm 0.1	43.3 \pm 3.7	2.1	0.8	35 \pm 5	116 \pm 15	10.281 \pm 0.033	0.214 \pm 0.053	-1.428	1.24	20.03	11.1 \pm 0.2
AGC 000233	0.01760	5.2 \pm 0.1	21.7 \pm 1.9	2.3	0.9	29 \pm 5	124 \pm 19	10.183 \pm 0.021	-0.010 \pm 0.061	-1.306	1.35	16.09	10.9 \pm 0.2
AGC 000247	0.03725	12.9 \pm 0.6	43.3 \pm 3.5	2.5	0.2	79 \pm 6	151 \pm 17	10.327 \pm 0.016	-0.036 \pm 0.031	-1.114	1.32	9.91	11.4 \pm 0.2
AGC 000252	0.01785	7.5 \pm 0.3	16.4 \pm 1.4	2.2	0.6	50 \pm 5	139 \pm 15	9.536 \pm 0.025	-0.812 \pm 0.056	-2.551	1.49	3.11	10.9 \pm 0.2
AGC 000317	0.01788	6.6 \pm 0.1	12.0 \pm 1.0	2.1	0.8	41 \pm 5	24 \pm 3	9.147 \pm 0.042	-0.836 \pm 0.053	-2.332	1.28	10.12	9.2 \pm 0.2
AGC 000401	0.01393	10.7 \pm 0.4	13.5 \pm 1.4	2.8	0.3	75 \pm 6	95 \pm 12	10.899 \pm 0.030	0.202 \pm 0.362	-0.437	1.41	20.36	10.4 \pm 0.2
AGC 000419	0.01461	12.4 \pm 0.2	21.0 \pm 2.3	1.9	0.7	49 \pm 5	139 \pm 15	10.531 \pm 0.017	-0.164 \pm 0.012	-0.608	1.22	36.25	11.0 \pm 0.2
AGC 000450	0.01788	10.6 \pm 0.2	25.3 \pm 5.7	2.7	0.6	52 \pm 5	217 \pm 26	11.020 \pm 0.013	-0.015 \pm 0.095	-1.891	1.71	0.76	11.4 \pm 0.2
AGC 000461	0.01392	6.8 \pm 0.1	30.2 \pm 6.8	2.4	0.6	52 \pm 5	170 \pm 18	10.521 \pm 0.024	0.207 \pm 0.065	-1.282	1.41	8.13	11.3 \pm 0.2
AGC 000463	0.01484	10.1 \pm 0.2	23.8 \pm 2.1	2.0	0.9	26 \pm 5	218 \pm 38	10.889 \pm 0.027	0.219 \pm 0.059	-0.529	1.21	18.13	11.4 \pm 0.2
AGC 000466	0.01814	6.5 \pm 0.1	17.4 \pm 4.0	2.4	0.4	65 \pm 5	121 \pm 13	9.730 \pm 0.028	-0.647 \pm 0.051	-2.074	1.44	2.58	10.8 \pm 0.2
AGC 000507	0.01757	16.3 \pm 1.4	36.2 \pm 7.5	2.5	0.2	90 \pm 5	198 \pm 22	10.746 \pm 0.032	-0.025 \pm 0.099	-1.396	1.52	6.53	11.5 \pm 0.2
AGC 000533	0.01825	7.4 \pm 0.1	21.2 \pm 4.4	2.0	0.3	72 \pm 5	143 \pm 15	9.849 \pm 0.024	-0.619 \pm 0.056	-2.188	1.40	5.45	11.0 \pm 0.2
AGC 000611	0.01814	8.2 \pm 0.1	29.7 \pm 2.6	2.3	1.0	13 \pm 5	345 \pm 134	10.444 \pm 0.020	0.339 \pm 0.044	-1.073	1.30	13.13	11.9 \pm 0.4

NOTE.—Col. (1): Galaxy name. Col. (2): Optical redshift from SDSS. Col. (3): Radius containing 90% of the Petrosian flux in the r band. Col. (4): H I radius calculated from the H I mass-size relation of Wang et al. (2016). Col. (5): Optical (r -band) concentration index C . Col. (6): Axis ratio in the r band. Col. (7): Optical inclination angle. Col. (8): Rotation velocity. Cols. (9)–(10): Stellar mass and SFR from spectral energy distribution fitting (Salim et al. 2018), scaled to the distance of ALFALFA. Cols. (11)–(13): SFR, $D_{\text{H}4000}$, and $\text{EW}(\text{H}\alpha)$ from the MPA-JHU catalog, calculated within the central $3''$ fiber of SDSS. SFR_{in} is scaled to the distance of ALFALFA and converted to the initial mass function of Chabrier (2003). Col. (14): Dynamical mass within $R_{\text{H}1}$. (This table is available in its entirety in machine-readable form.)

REFERENCES

- Adams, E., Adebahr, B., de Blok, W. J. G., et al. 2018, *BAAS*, 231, 354.04
- Ahumada, R., Prieto, C. A., Almeida, A., et al. 2020, *ApJS*, 249, 3
- Andersen, D. R., & Bershad, M. A. 2009, *ApJ*, 700, 1626
- Ashley, T., Simpson, C. E., Elmegreen, B. G., Johnson, M., & Pokhrel, N. R. 2017, *AJ*, 153, 132
- Astropy Collaboration, Robitaille, T. P., Tollerud, E. J., et al. 2013, *A&A*, 558, A33
- Baldwin, J. E., Lynden-Bell, D., & Sancisi, R. 1980, *MNRAS*, 193, 313
- Balogh, M. L., Morris, S. L., Yee, H. K. C., Carlberg, R. G., & Ellingson, E. 1999, *ApJ*, 527, 54
- Barnes, J. E. 2002, *MNRAS*, 333, 481
- Bok, J., Blyth, S. L., Gilbank, D. G., & Elson, E. C. 2019, *MNRAS*, 484, 582
- Boomsma, R., Oosterloo, T. A., Fraternali, F., van der Hulst, J. M., & Sancisi, R. 2005, *A&A*, 431, 65
- Bottinelli, L., Gougouenheim, L., Fouque, P., & Paturel, G. 1990, *A&AS*, 82, 391
- Bournaud, F., Combes, F., Jog, C. J., & Puerari, I. 2005, *A&A*, 438, 507
- Brinchmann, J., Charlot, S., White, S. D. M., et al. 2004, *MNRAS*, 351, 1151
- Brosch, N., Spector, O., & Zitrin, A. 2011, *MNRAS*, 415, 431
- Cameron, E. 2011, *PASA*, 28, 128
- Catinella, B., Saintonge, A., Janowiecki, S., et al. 2018, *MNRAS*, 476, 875
- Catinella, B., Schiminovich, D., & Kauffmann, G. 2008, in *AIP Conf. Ser., The Evolution of Galaxies Through the Neutral Hydrogen Window*, ed. R. Minchin & E. Momjian (Melville, NY: AIP), 252
- Catinella, B., Schiminovich, D., Cortese, L., et al. 2013, *MNRAS*, 436, 34
- Catinella, B., Schiminovich, D., Kauffmann, G., et al. 2010, *MNRAS*, 403, 683
- Catinella, B., Schiminovich, D., Kauffmann, G., et al. 2012, *A&A*, 544, A65
- Chabrier, G. 2003, *PASP*, 115, 763
- Cortese, L., Catinella, B., Boissier, S., Boselli, A., & Heinis, S. 2011, *MNRAS*, 415, 1797
- Cortese, L., Catinella, B., & Smith, R. 2021, *PASA*, 38, e035
- Courteau, S. 1997, *AJ*, 114, 2402
- Courtois, H. M., Tully, R. B., Fisher, J. R., et al. 2009, *AJ*, 138, 1938
- Deg, N., Blyth, S. L., Hank, N., Kruger, S., & Carignan, C. 2020, *MNRAS*, 495, 1984
- Dewdney, P. E., Hall, P. J., Schilizzi, R. T., & Lazio, T. J. L. W. 2009, *IEEEP*, 97, 1482
- Dickel, J. R., & Rood, H. J. 1978, *ApJ*, 223, 391
- Djorgovski, S. G., Gal, R. R., Odewahn, S. C., et al. 1998, in *Wide Field Surveys in Cosmology*, ed. S. Colombi, Y. Mellier, & B. Raban (Gif-sur-Yvette: Editions Frontieres), 89
- Durbala, A., Finn, R. A., Crone Odekon, M., et al. 2020, *AJ*, 160, 271
- Dutton, A. A., Obreja, A., & Macciò, A. V. 2019, *MNRAS*, 482, 5606
- El-Badry, K., Bradford, J., Quataert, E., et al. 2018, *MNRAS*, 477, 1536
- Ellison, S. L., Patton, D. R., Simard, L., et al. 2010, *MNRAS*, 407, 1514
- Ellison, S. L., Patton, D. R., Simard, L., & McConnachie, A. W. 2008, *AJ*, 135, 1877
- Espada, D., Verdes-Montenegro, L., Huchtmeier, W. K., et al. 2011, *A&A*, 532, A117
- Fumagalli, M., Patel, S. G., Franx, M., et al. 2012, *ApJL*, 757, L22
- Geha, M., Blanton, M. R., Masjedi, M., & West, A. A. 2006, *ApJ*, 653, 240
- Giese, N., van der Hulst, T., Serra, P., et al. 2016, *MNRAS*, 461, 1656
- Giovanelli, R., Haynes, M. P., Kent, B. R., et al. 2007, *AJ*, 133, 2569
- Hallenbeck, G., Papastergis, E., Huang, S., et al. 2012, *AJ*, 144, 87
- Hayashi, E., & Navarro, J. F. 2006, *MNRAS*, 373, 1117
- Haynes, M. P., Giovanelli, R., Kent, B. R., et al. 2018, *ApJ*, 861, 49
- Haynes, M. P., Giovanelli, R., Martin, A. M., et al. 2011, *AJ*, 142, 170
- Haynes, M. P., Hogg, D. E., Maddalena, R. J., Roberts, M. S., & van Zee, L. 1998, *AJ*, 115, 62
- Hess, K. M., Cluver, M. E., Yahya, S., et al. 2017, *MNRAS*, 464, 957
- Ho, L. C., Darling, J., & Greene, J. E. 2008a, *ApJS*, 177, 103
- Ho, L. C., Darling, J., & Greene, J. E. 2008b, *ApJ*, 681, 128
- Huang, S., Haynes, M. P., Giovanelli, R., & Brinchmann, J. 2012, *ApJ*, 756, 113
- Hubble, E. P. 1926, *ApJ*, 64, 321
- Huchtmeier, W. K., Karachentsev, I. D., Karachentseva, V. E., Kudrya, Y. N., & Mitronova, S. N. 2005, *A&A*, 435, 459
- Jog, C. J., & Solomon, P. M. 1992, *ApJ*, 387, 152
- Johnston, S., Bailes, M., Bartel, N., et al. 2007, *PASA*, 24, 174
- Jones, M. G., Verdes-Montenegro, L., Damas-Segovia, A., et al. 2019, *A&A*, 632, A78
- Kauffmann, G., Heckman, T. M., White, S. D. M., et al. 2003, *MNRAS*, 341, 33
- Kenney, J. D. P., Abramson, A., & Bravo-Alfaro, H. 2015, *AJ*, 150, 59
- Khostovan, A. A., Malhotra, S., Rhoads, J. E., et al. 2021, *MNRAS*, 503, 5115

- Koribalski, B. S., Staveley-Smith, L., Kilborn, V. A., et al. 2004, *AJ*, 128, 16
- Koribalski, B. S., Staveley-Smith, L., Westmeier, T., et al. 2020, *Ap&SS*, 365, 118
- Laine, S., & Gottesman, S. T. 1998, *MNRAS*, 297, 1041
- Lambas, D. G., Tissera, P. B., Alonso, M. S., & Coldwell, G. 2003, *MNRAS*, 346, 1189
- Leisman, L., Rhode, K. L., Ball, C., et al. 2021, *AJ*, 162, 274
- Lelli, F., McGaugh, S. S., & Schombert, J. M. 2016, *AJ*, 152, 157
- Lineweaver, C. H., Tenorio, L., Smoot, G. F., et al. 1996, *ApJ*, 470, 38
- Mármol-Queralto, E., McLure, R. J., Cullen, F., et al. 2016, *MNRAS*, 460, 3587
- Martinsson, T. P. K., Verheijen, M. A. W., Bershad, M. A., et al. 2016, *A&A*, 585, A99
- Masters, K. L. 2005, PhD Thesis, Cornell University, United States
- Matthews, L. D., van Driel, W., & Gallagher III, J. S. 1998, *AJ*, 116, 1169
- McGlynn, T., & Scollick, K. 1994, in *ASP Conf. Ser.* 61, *Astronomical Data Analysis Software and Systems III*, ed. D. R. Crabtree, R. J. Hanisch, & J. Barnes (San Francisco, CA: ASP), 34
- Mei, S., Blakeslee, J. P., Côté, P., et al. 2007, *ApJ*, 655, 144
- Meyer, M. J., Zwaan, M. A., Webster, R. L., et al. 2004, *MNRAS*, 350, 1195
- Morganti, R. 2017, *Frontiers in Astronomy and Space Sciences*, 4, 42
- Morganti, R., de Zeeuw, P. T., Oosterloo, T. A., et al. 2006, *MNRAS*, 371, 157
- Nan, R., Li, D., Jin, C., et al. 2011, *International Journal of Modern Physics D*, 20, 989
- Newnham, L., Hess, K. M., Masters, K. L., et al. 2020, *MNRAS*, 492, 4697
- Patton, D. R., Carlberg, R. G., Marzke, R. O., et al. 2000, *ApJ*, 536, 153
- Pier, J. R., Munn, J. A., Hindsley, R. B., et al. 2003, *AJ*, 125, 1559
- Reynolds, T. N., Westmeier, T., & Staveley-Smith, L. 2020, *MNRAS*, 499, 3233
- Richter, O. G., & Sancisi, R. 1994, *A&A*, 290, L9
- Roberts, M. S. 1962, *AJ*, 67, 437
- Roberts, M. S. 1978, *AJ*, 83, 1026
- Robertson, B., Bullock, J. S., Cox, T. J., et al. 2006, *ApJ*, 645, 986
- Saha, K., Combes, F., & Jog, C. J. 2007, *MNRAS*, 382, 419
- Saintonge, A. 2007, *AJ*, 133, 2087
- Saintonge, A., & Catinella, B. 2022, *ARA&A*, in press
- Salim, S., Boquien, M., & Lee, J. C. 2018, *ApJ*, 859, 11
- Sánchez-Janssen, R., Méndez-Abreu, J., & Aguerri, J. A. L. 2010, *MNRAS*, 406, L65
- Sancisi, R., Fraternali, F., Oosterloo, T., & van der Hulst, T. 2008, *A&A Rv*, 15, 189
- Scott, T. C., Bravo-Alfaro, H., Brinks, E., et al. 2010, *MNRAS*, 403, 1175
- Scott, T. C., Brinks, E., Cortese, L., Boselli, A., & Bravo-Alfaro, H. 2018, *MNRAS*, 475, 4648
- Shostak, G. S. 1977, *A&A*, 58, L31
- Sorgho, A., Hess, K., Carignan, C., & Oosterloo, T. A. 2017, *MNRAS*, 464, 530
- Springob, C. M., Haynes, M. P., Giovanelli, R., & Kent, B. R. 2005, *ApJS*, 160, 149
- Springob, C. M., Masters, K. L., Haynes, M. P., Giovanelli, R., & Marinoni, C. 2007, *ApJS*, 172, 599
- Stewart, I. M., Blyth, S. L., & de Blok, W. J. G. 2014, *A&A*, 567, A61
- Strateva, I., Ivezić, Ž., Knapp, G. R., et al. 2001, *AJ*, 122, 1861
- Tifft, W. G., & Cocke, W. J. 1988, *ApJS*, 67, 1
- Tully, R. B., Courtois, H. M., Dolphin, A. E., et al. 2013, *AJ*, 146, 86
- Tully, R. B., & Fisher, J. R. 1977, *A&A*, 54, 661
- Verheijen, M. A. W., & Sancisi, R. 2001, *A&A*, 370, 765
- Wang, J., Catinella, B., Saintonge, A., et al. 2020, *ApJ*, 890, 63
- Wang, J., Koribalski, B. S., Serra, P., et al. 2016, *MNRAS*, 460, 2143
- Watts, A. B., Catinella, B., Cortese, L., & Power, C. 2020, *MNRAS*, 492, 3672
- Westmeier, T., Jurek, R., Obreschkow, D., Koribalski, B. S., & Staveley-Smith, L. 2014, *MNRAS*, 438, 1176
- Wong, O. I., Ryan-Weber, E. V., Garcia-Appadoo, D. A., et al. 2006, *MNRAS*, 371, 1855
- York, D. G., Adelman, J., Anderson, John E., J., et al. 2000, *AJ*, 120, 1579
- Yu, N., Ho, L. C., & Wang, J. 2020, *ApJ*, 898, 102
- Yu, N., Wang, J., & Ho, L. C. 2022, *ApJ*, submitted
- Zhang, C., Peng, Y., Ho, L. C., et al. 2019, *ApJL*, 884, L52
- Zhou, Z., Wu, H., Zhou, X., & Ma, J. 2018, *PASP*, 130, 094101
- Zuo, P., Ho, L. C., Wang, J., Yu, N., & Shangguan, J. 2022, *ApJ*, in press